

53rd SME North American Manufacturing Research Conference (NAMRC 53, 2025)

## An Analytical Model Integrating Tool Kinematics and Material Flow for the Spindle Torque Prediction in Additive Friction Stir Deposition

Jiajie Wu<sup>a,b</sup>, Mason Ma<sup>a,b</sup>, Jaydeep Karandikar<sup>c</sup>, Christopher Tyler<sup>c</sup>, Tony Shi<sup>a,b,\*</sup>, Tony Schmitz<sup>b,c</sup>

<sup>a</sup>Manufacturing Mind&Physics Laboratory, University of Tennessee Knoxville, Knoxville, TN 37996, USA

<sup>b</sup>Machine Tool Research Center, University of Tennessee Knoxville, Knoxville, TN 37996, USA

<sup>c</sup>Manufacturing Science Division, Oak Ridge National Laboratory, Oak Ridge, TN 37830, USA

\* Corresponding author. Tel.: +1-865-974-7654; E-mail address: tony.shi@utk.edu

### Abstract

Understanding the relationship between spindle torque, tool kinematics, and material flow is important for the emerging solid-state additive friction stir deposition (AFSD) process. This study presents the first analytical modeling effort to integrate tool kinematics and material flow for the spindle torque prediction in AFSD. In the proposed model, material flow is first inferred by tool kinematics with consideration of slippage. The derived strain rate is then used to calculate flow stress based on the Johnson-Cook constitutive models for different materials. Spindle torque is estimated by integrating the effects of plastic deformation and sliding friction across tool-deposition surface. Experiments of wall deposition using aluminium 7075 feedstock at different spindle speeds are performed. In addition to aluminium 7075, the experimental data of stainless steel 316 in the literature is also applied for model validation. Experimental validation results show that the proposed analytical model can achieve good performance of spindle torque prediction for different deposition materials in AFSD.

© 2025 The Authors. Published by ELSEVIER Ltd. This is an open access article under the CC BY-NC-ND license (<https://creativecommons.org/licenses/by-nc-nd/4.0>)

Peer-review under responsibility of the scientific committee of the NAMRI/SME.

**Keywords:** additive friction stir deposition; analytical model; spindle torque; tool kinematics; material flow

### 1. Introduction

Additive friction stir deposition (AFSD) is an emerging solid-state additive manufacturing process. It has several advantages over fusion-based metal additive manufacturing, including lower energy consumption, lower porosity, high build rate, and capability of manufacturing large parts [1, 2]. The applications of AFSD for aluminium matrix composites [3, 4], material recycling [5], repair [6], and hybrid manufacturing [7, 8] have been explored.

The AFSD process is illustrated in Figure 1. AFSD utilizes frictional heating, compression, and shear to generate a thin layer of plastic material flow [9]. The desired geometry is manufactured via layer-by-layer depositions. The critical process parameters are the spindle speed and traverse speed of tool, and material feed rate in AFSD. The spindle and traverse speeds determine tool kinematics and drive the frictional

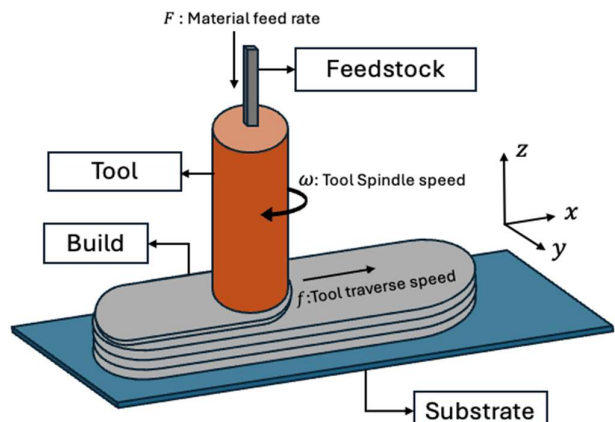


Figure 1: Schematic illustration of AFSD process.

heating and shear to generate material flow. The material flow and thermal history determine the microstructure evolution of deposition. Previous research efforts have studied the material microstructure evolution and property [10–18]. Significant modeling efforts have been made to understand the physical process of AFSD, including numerical modeling [19–22], physics-informed machine learning modeling [23–25], and analytical modeling [26]. However, these existing models cannot be used for spindle torque prediction in AFSD.

Spindle torque, as a critical physical variable in AFSD, is highly sensitive to material plastic deformation and contact conditions at the tool-deposition surface, compared with temperature. Spindle speed is influenced by spindle torque applied to tool and the resistance encountered from material. By linking material flow behaviour with spindle torque, precise control of tool kinematics has the potential to be achieved, that can further reduce variations and promote more uniform deformation during the AFSD process. To the best of the authors' knowledge, only a few qualitative relationships between spindle torque, spindle speed, and temperature are summarized based on experimental observations [27–29].

This study presents the first analytical modeling effort to integrate tool kinematics and material flow for spindle torque prediction at the steady state in AFSD. In the proposed model, material flow is inferred by tool kinematics with consideration of slippage. The derived strain rate is then used to calculate flow stress based on the Johnson-Cook constitutive model for different materials. Spindle torque can therefore be estimated by integrating the effects of plastic deformation and sliding friction across tool-deposition surface. Experimental data of aluminium 7075 (Al7075) and stainless steel 316 (SS316) is used to validate the proposed analytical model. Validation results show that the proposed analytical model can achieve good performance of spindle torque prediction for different deposition materials in AFSD.

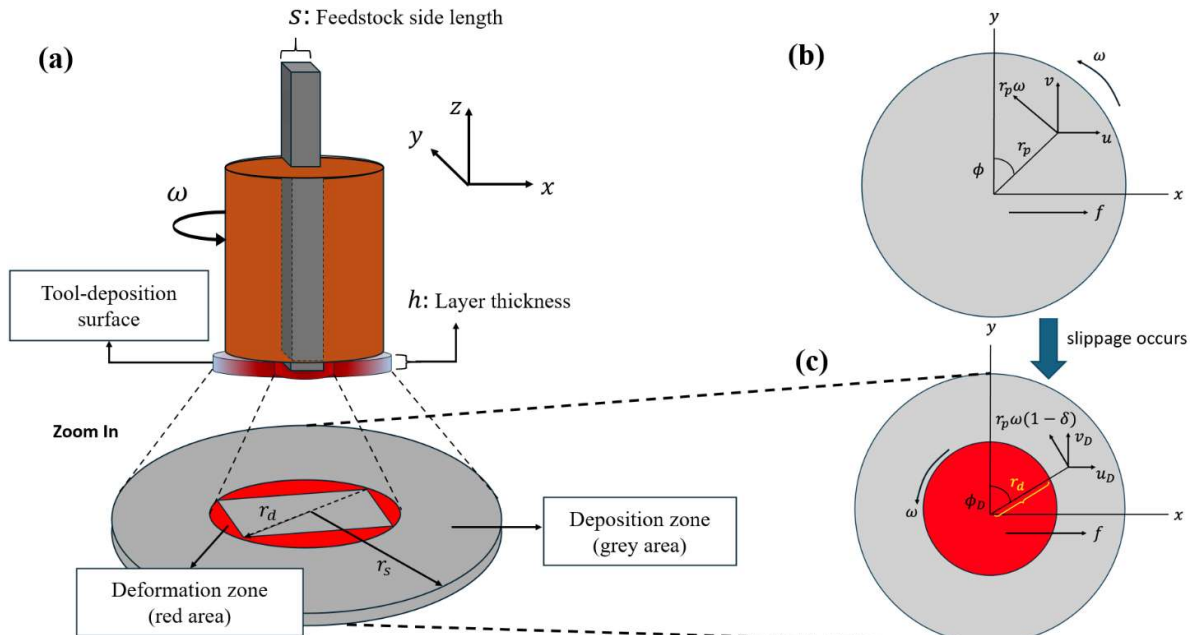


Figure 2: Illustration of tool-deposition surface. The material flow is simplified as the circular shape with specified height. (a) Zoom in of the tool-deposition surface. (b) Rotating-translating tool kinematics. Spindle rotation is counterclockwise and tool feed velocity is to the right. (c) Upper surface of material flow.

This paper is organized as follows. Section 2 presents the proposed analytical model. Section 3 describes the experimental setup. Section 4 presents the numerical results of model validation on Al7075. Section 5 provides additional validations with a different material SS316 in the literature. Section 6 concludes this paper.

## 2. Proposed Spindle Torque Model

The proposed spindle torque model is developed in two steps: 1) link tool kinematics to material flow with consideration of slippage (Section 2.1); and 2) link the flow stress to spindle torque by considering the combined effect of plastic deformation and sliding friction based on analyses of equilibrium and contact condition (Section 2.2).

The model development of this study assumes sufficient material flow in AFSD, that means the deposited material has been effectively softened and dragged by the tool. This assumption is reasonable and desired in practice, as the slippage and insufficient stirring caused by improper process conditions can lead to undesirable material properties. Some strategies based on experimental data to determine whether the material flow is sufficiently generated or not are given for model validation (Section 4.1).

Focusing on the tool-deposition surface in AFSD as shown in Figure 2, the main idea of the proposed model design is summarized as follows. Material flow is represented as a circular shape with a specified height. The area under the feedstock and tool shoulder exhibits different physical processes. The region right beneath the feedstock, marked in red, can be described as the deformation zone [13]. At this zone, the material starts to yield, and undergoes severe plastic deformation caused by the normal force from material extrusion and the shear generated by tool rotation [30]. In addition, the area marked in grey is the deposition zone, where

a combined effect of plastic deformation and sliding friction between tool shoulder and surface of material flow occurs. This study distinguishes between the two regions to establish the spindle torque prediction model in AFSD.

## 2.1 Link Tool Kinematics to Material Flow

This study assumes that spindle torque is independent of layer thickness. The upper surface of material flow is inferred from tool kinematics following the previous work [26]. The tool kinematics is introduced in Figure 2. The tool traverse speed  $f$  is on the  $x$  direction. The tool rotates counterclockwise with a time dependent rotation angle  $\phi$ .  $r_p$  is the radius at which the force acts.  $u$  and  $v$  are velocity components of the tool. The upper surface of material flow corresponding to tool kinematics is displayed in Figure 2(c).

In the deformation zone, a fully sticking condition is assumed, as the feedstock is grabbed by the tool. For the deposition zone, slippage is expected when a hard tool acts on softened materials. By considering slippage, Eq. (1) provides the associated displacement and velocity of material flow at radius  $r_p$  in the deposition zone.

$$\phi_D(t) = \phi_0 + (1 - \delta)\Omega t, \quad (1a)$$

$$x_D(r_p, t) = r_p \sin \phi_D + (1 - \delta)ft, \quad (1b)$$

$$y_D(r_p, t) = r_p \cos \phi_D, \quad (1c)$$

$$u_D(r_p, t) = (1 - \delta)(-r_p \omega \cos \phi_D + f), \quad (1d)$$

$$v_D(r_p, t) = (1 - \delta)r_p \omega \sin \phi_D. \quad (1e)$$

$\phi_0$  is the initial tool rotation angle and can be set as 0.  $\Omega$  is the angular velocity ( $^{\circ}/s$ ) corresponding to the given spindle speed  $\omega$  (in rad/s).  $\phi_D$  represents the rotating angle of material flow, which is utilized to calculate the current displacements  $x_D$  and  $y_D$ , and the velocity components  $u_D$  and  $v_D$  of material flow.

Garcia et al. have observed the radially increasing trend of slippage when a H13 tool steel print head processes the deposited material AA6061 [31]. The slip rate is hereby defined as an exponential growth function of spindle speed  $\omega$  and radial  $r_p$  [13].

$$\delta = 1 - e^{-\frac{-\delta_0 \omega (r_p - r_d)}{\omega_0 (r_s - r_d)}}. \quad (2)$$

In Eq. (2),  $\delta_0$  is a scaling constant, and  $\omega_0$  is the reference value for spindle speed. These values can be adjusted to change the spatial distribution of slippage.

The effective strain rate  $\dot{\epsilon}_e$  is determined with material flow in Eq. (1), strain rate tensor  $E$ , and gradient of velocity  $L$ . Effective strain rate  $\dot{\epsilon}_e$  at location  $r_p$  is calculated with Eq. (3),

$$\dot{\epsilon}_e(r_p) = \sqrt{\frac{2}{3} \langle E(r_p), E(r_p) \rangle}, \quad (3)$$

where  $\langle E(r_p), E(r_p) \rangle$  represents the Frobenius inner product.

The strain rate tensor  $E$  at location  $r_p$  is obtained by Eq. (4), and the gradient of velocity  $L$  is defined in Eq. (5).  $L$  can be calculated by utilizing the numerical differential method based on Eq. (1) for one revolution of tool,  $\phi$  is varied from 0 to  $2\pi$ .

$$E(r_p) = \frac{1}{2} (L(r_p) + L^T(r_p)), \quad (4)$$

$$L = \begin{bmatrix} \frac{du_D}{dx_D} & \frac{du_D}{dy_D} \\ \frac{dv_D}{dx_D} & \frac{dv_D}{dy_D} \end{bmatrix}. \quad (5)$$

The resultant effective strain rate is obtained by averaging the strain rate from each revolution step with Eqs. (3-5).

Material flow stress is estimated by Johnson-Cook (J-C) constitutive model provided in Eq. (6). It describes the thermal softening, strain hardening, and strain rate hardening of the material.

$$\sigma = (A + B \epsilon^n) \left( 1 + C \ln \frac{\dot{\epsilon}}{\dot{\epsilon}_0} \right) \left( 1 - \left( \frac{T - T_0}{T_m - T_0} \right)^m \right). \quad (6)$$

$A$ ,  $B$ ,  $C$ ,  $m$ , and  $n$  are model parameters obtained from experiments of the selected material.  $T_0$  is the reference temperature and generally set as room temperature.  $T_m$  is the melting temperature of the material. The J-C model parameters for Al7075 are shown in Table 1.

Table 1: J-C model parameters for Al7075 [32-38].

Model	$A$ (MPa)	$B$ (MPa)	$C$	$n$	$m$	$T_m$ (°C)	$\dot{\epsilon}_0$ ( $s^{-1}$ )
1	520	477	0.001	0.52	1	619.85	0.0005
2	527	575	0.017	0.72	1.61	619.85	1
3	546	678	0.024	0.71	1.56	619.85	1
4	517	405	0.0075	0.41	1.1	619.85	0.000161
5	452.4	457.1	0.0109	0.357	1.131	619.85	1
6	448.454	475.808	0.0012	0.394	1.29	619.85	0.0001
7	665.6	72.6	0.002	0.48	0.79	635	1
8	496	310	0	0.41	1.2	635	1
9	435.7	534.624	0.019	0.504	0.97	619.85	1

The equivalent plastic strain  $\epsilon$  in Eq. (6) is calculated with Eq. (7) as the ratio of the extruded cross-section area  $A_1$  and cross-section area  $A_0$  of feedstock.

$$\epsilon = \ln \frac{A_1}{A_0} = \ln \frac{2\pi r_f h}{s^2}, \quad (7)$$

where the radius  $r_f = 0.5r_s$  is set as half of the tool deposition radius [26].

## 2.2 Link Material Flow to Spindle Torque

The primary components contribute to steady-state spindle torque including the idle torque  $M_{idle}$  related to internal gears and bearings, the material's resistance to deformation  $M_{bulk deformation}$ , and the sliding friction at tool-deposition surface  $M_{interface}$  [39], as shown in Eq. (8).

$$M_{spindle} - M_{idle} = M_{bulk deformation} + M_{interface}. \quad (8)$$

$M_{idle}$  can either be obtained from measurements or neglected when the feedstock material exhibits high resistance to deformation. By simplifying the tool geometry as a flat plane,  $M_{bulk deformation}$  and  $M_{interface}$  are combined and approximated by assuming the torque is responding to friction force at upper surface of material flow. In addition, the proposed model assumes the contact condition is stable.

The combined torque of  $M_{bulk deformation}$  and  $M_{interface}$  in Eq. (8) is denoted as  $T_f^*$ . To distinguish between the different physical processes occurring in the deformation and deposition zones,  $T_f^*$  is estimated by separately considering the torque in each zone and then combining the results, as shown in Eq. (9).

$$\begin{aligned} T_f^* &= M_{spindle} - M_{idle} \\ &= T_f^{Deformation} + T_f^{Deposition}. \end{aligned} \quad (9)$$

The torques at deformation and deposition zones are correspondingly calculated as follows.

**Torque at deformation zone.** Tresca friction is assumed to be dominant at deformation region where the rotating tool mainly experiences material's resistance to deformation.

$$\begin{aligned} T_f^{Deformation} &= \oint_{A_d} r \times \tau (dA_d) \\ &= \int_0^{2\pi} \int_0^{r_d} r \times \tau (r dr d\theta). \end{aligned} \quad (10)$$

In Eq. (10),  $A_d$  is the area ( $\text{m}^2$ ) of the deformation zone,  $r$  is the radius (m) at which the friction force acts, and  $\tau$  is the shear stress (MPa). Due to the rotation of feedstock, the deformation zone is defined to be the circular area with radius  $r_d$  of  $\sqrt{2}s/2$ , where  $s$  is the feedstock side length.

Eq. (11) provides the shear stress under sticking condition.

$$\tau = \frac{\sigma_{yield}}{\sqrt{3}}. \quad (11)$$

$\sigma_{yield}$  is the temperature-dependent material yield strength (MPa). A polynomial model was used to predict  $\sigma_{yield}$ . The model is fitted with the experimental data of Al7075 in [40].

Note that temperature can vary across the cross-section of feedstock, leading to non-uniform stress and strain distributions. The effective radius  $r_e$  is applied to account for such inhomogeneity, and its value is set to be  $0.724r_d$  by [41]. It mitigates the impact of local variations by focusing on the overall behavior of material. Thus, Eq. (10) is reformulated as Eq. (12).

$$T_f^{Deformation} = \frac{2\pi r_e^3}{3}. \quad (12)$$

**Torque at deposition zone.** Considering combined plastic deformation and sliding friction at deposition zone, the weighted Tresca friction and Coulomb friction are applied to approximate  $T_f^{Deposition}$  [42, 43], as shown in Eq. (13).

$$\begin{aligned} T_f^{Deposition} &= \oint_{A_s} r \times ((1-\delta)\tau_p + \delta\mu P_N) (dA_s) \\ &= \int_0^{2\pi} \int_{r_d}^{r_s} r \times ((1-\delta)\tau_p + \delta\mu P_N) (r dr d\theta). \end{aligned} \quad (13)$$

In Eq. (13),  $A_s$  is the area of deposition zone, and  $\tau_p$  is the shear stress related to material plastic deformation. The Coulomb friction is proportional to the normal direction force  $P_N$  with friction coefficients  $\mu$ . The slip rate  $\delta$  is initially proposed as an indicator of contact conditions under the context of friction stir welding [44], which has also been applied to leverage heat generation at tool-deposition surface due to friction and plastic work in AFSD [13, 20, 21].  $\delta = 0$  indicates fully sticking, where material flow moves at the same velocity as tool. When  $\delta = 0$ , the friction force is considered only related to the material plastic deformation due to shear.

Both Tresca and Coulomb frictions are approximated by flow stress  $\sigma$ . Therefore, Eq. (13) is reformulated as Eq. (14).

$$T_f^{Deposition} = \int_0^{2\pi} \int_{r_d}^{r_s} r \times \eta \left( (1-\delta) \frac{\sigma}{\sqrt{3}} + \delta\mu\sigma \right) (r dr d\theta). \quad (14)$$

The scaling factor  $\eta$  is introduced to mitigate the estimation error of constitutive model and Coulomb friction. A better estimation of the normal stress will improve the prediction accuracy.

## 2.3 Algorithm of Spindle Torque Prediction

The proposed model predicts the steady-state spindle torque with the temperature at tool head and tool kinematics under given spindle and traverse speeds. It should be noted that due to the strongly coupled relationship between tool kinematics and temperature, the mismatching between these inputs can lead to incorrect results. In addition, another model to link process parameters and steady-state temperature will enable off-line prediction capabilities of the proposed model.

To initialize the model, three parameters need to be determined with experimental data:  $\delta_0$ ,  $\omega_0$ , and the scaling factor  $\eta$ . Although trial and error is needed, limited attempts

are required by fixing the reference spindle speed  $\omega_0$  at first and then adjusting  $\delta_0$  and  $\eta$ . The initialized model predicts the spindle torque with the following steps:

1. Determine the tool kinematics by providing spindle and traverse speeds.
2. Calculate the torque at deformation zone with temperature-dependent material yield strength from experimental data and Eqs. (11-12).
3. Calculate the torque at deposition zone. Firstly, determine the slip rate in Eq. (2), and the mean strain rate at each location is computed over one tool revolution with Eqs. (3-5); Secondly, compute the flow stress at each location with Johnson-Cook constitutive model for given temperature. Lastly, estimate the torque with Eq. (14). The integral is computed numerically based on Gauss-Kronrod quadrature method [45].
4. Combine the torque in two regions as in Eq. (9) and the spindle torque is obtained by Eq. (8).

### 3. Experimental Setup

The wall geometry was deposited via AFSD process under different process conditions as listed in Table 3. For each set of process parameters, 30 layers were deposited. Experiments were performed with a commercially available AFSD machine as shown in Figure 3(a). The 38.1 mm diameter tool for deposition is made of copper beryllium (CuBe) and has an H13 tool steel cap with four 2.3 mm tall shoulder protrusions. The tool included a 12.7 mm square bore to constrain the feedstock. A thermocouple module for tool temperature measurement was installed offset from the tool center and located axially 0.25 mm to 0.38 mm from the tool face. The sampling rate of the thermocouple was 1 Hz. The recorded temperature could be used for closed-loop control, where the spindle speed could be adjusted to maintain the desired temperature. The closed-loop temperature control was disabled in the experiments such that the wall geometry was deposited with a fixed spindle speed. The feedstock for deposition was Al7075 and the deposition was done on Al7075-T651 build plate.

The spindle speeds selected were 105, 115, 125, and 135 RPM, with fixed setpoint of material feed velocity  $F = 65$

mm/min, tool traverse speed  $f = 127$  mm/min, and layer thickness  $h = 1.5$  mm. The deposition was conducted in a single direction as shown in Figure 3 (b). When the deposition of one layer was finished, the tool returned to the start point before depositing the next layer. For better bonding between the first layer deposition and the substrate, the tool traverse speed and material feed rate were 50% of the commanded setpoints. The deposited wall is shown in Figure 3 (c-d). The width of the deposition was measured as 54.1 mm.

Table 3: Process parameters for AFSD with Al7075 feedstocks.

Experiment	Spindle speed (RPM)	Traverse speed (mm/min)	Material feed rate (mm/min)	Layer thickness (mm)
1	105	127	65	1.5
2	115	127	65	1.5
3	125	127	65	1.5
4	135	127	65	1.5

### 4. Model Validation

#### 4.1 Computational Setup

*Validation data preprocessing.* The data with a time window of 40 seconds at the steady-state deposition of the second layer is selected for model validation, as shown in Figure 4. This is because the first layer was deposited at 50% of the commanded feedstock and tool feed velocities. Based on the experimental data, two strategies used to distinguish whether the material flow is sufficiently generated or not are given as follows.

- *Strategy 1: Deviation of steady-state spindle torque in adjacent deposition layers.* Previous studies have identified a transition in contact conditions, where either sticking or sliding friction dominates based on the deposition temperature [46, 47]. At lower temperature, sliding friction prevails as the material is not sufficiently softened to be effectively dragged by the tool. The transition from sliding to sticking condition occurs with increased temperature. Therefore, insufficient material flow can be identified if there is a drastic increase in spindle torque during multi-layer deposition (The

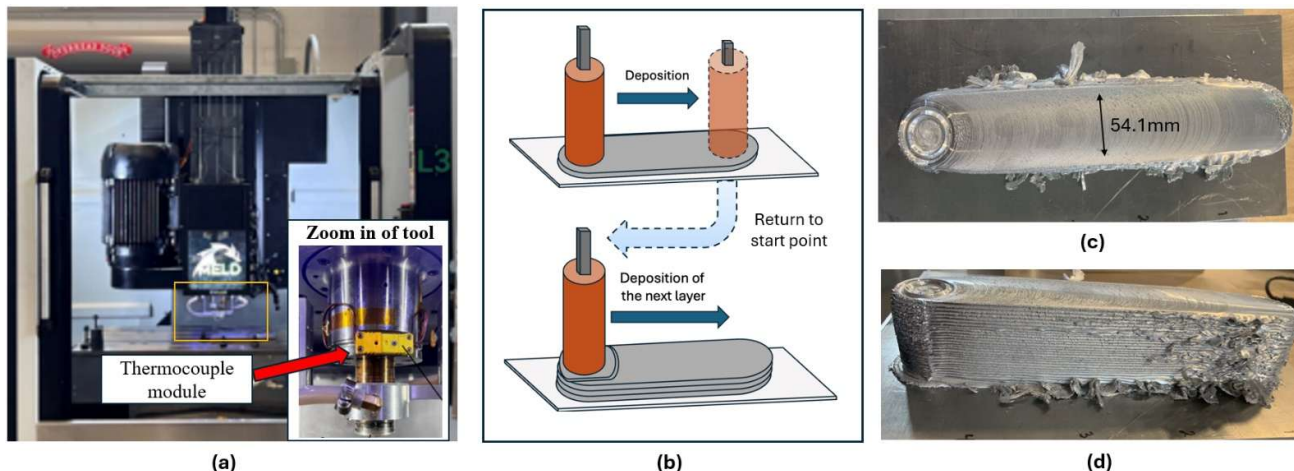


Figure 3: Overview of experimental setup. (a) The AFSD machine. One thermocouple was installed on the tool to measure the tool head temperature. (b) The procedure of depositing a wall geometry. The tool returned to the start point once the deposition of one layer was done. (c) The bottom view of the deposited wall. The deposition width was approximately 54.1 mm. (d) The side view of deposition.

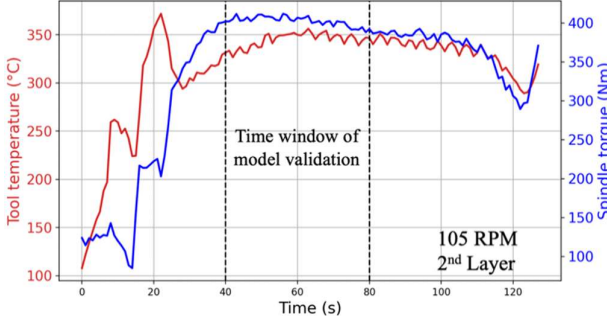


Figure 4: Time window for model validation. The time window is 40 seconds at the steady-state deposition when the spindle speed is stable around the setpoint.

deposition temperature will generally increase for a small wall geometry due to heat accumulation). This drastic increase in torque mainly occurs due to a significantly higher flow stress compared to the Coulomb friction force because the tool does not apply intensive external pressure on the material flow.

- *Strategy 2: Ratio of spindle speed over traverse speed.* Insufficient material flow can be identified by analysing the sensitivity in deposition width for a given spindle speed and material feed rate under different traverse speeds. The excessive sliding can be inferred if the deposition width is significantly reduced, which means the material is not sufficiently stirred and spread.

According to these two strategies, experimental data is divided into two groups: (1) Sufficiently generated material flow (SGMF); and (2) Not sufficiently generated material flow (NSGMF). Note that only group SGMF satisfies the model assumption and is used for model validation, but the prediction results on group NSGMF are also displayed in Figures 7 and 9.

*Model parameter setting.* The parameters for the model are shown in Table 4. The geometry of tool-deposition surface is determined from the parameters of AFSD machine tool and width of the deposited wall.

Table 4: Experimental setting and parameters applied for model validation (Al7075).

Description	Notation	Numerical Values
Spindle speed (RPM)	$\omega$	{105, 115, 125, 135}
Tool traverse speed (mm/min)	$f$	127
Tool deposition radius (mm)	$r_s$	27.05
Feedstock bar side length (mm)	$s$	12.7
Deformation zone radius (mm)	$r_d$	$\sqrt{2}s/2$
Deposition height (mm)	$h$	1.5
Initial temperature (°C)	$T_0$	25
Friction coefficients	$\mu$	0.25
Reference slip factor	$\delta_0$	1.5
Reference spindle speed (RPM)	$\omega_0$	100
Scaling factor	$\eta$	0.11

*Computational environment.* All simulation experiments are deployed on a workstation with AMD Ryzen Threadripper PRO 5975WX 32-Cores 3.60 GHz, 128 GB memory, 64-bit Windows 11 Pro operating system. The model's computation time is 1.17 seconds to generate all the results in Section 4.2, comprising a total of 1,080 predictions.

## 4.2 Results and Analyses of Spindle Torque Prediction

This section validates the proposed spindle torque model using experimental data. The results are analyzed and

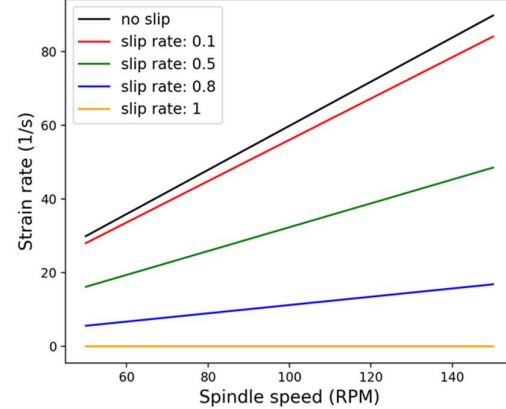


Figure 5: Spindle speed-strain rate curve under different slip rates. The strain rate at the outer edge of the deposition zone is computed for various slip rates for illustrative purposes.

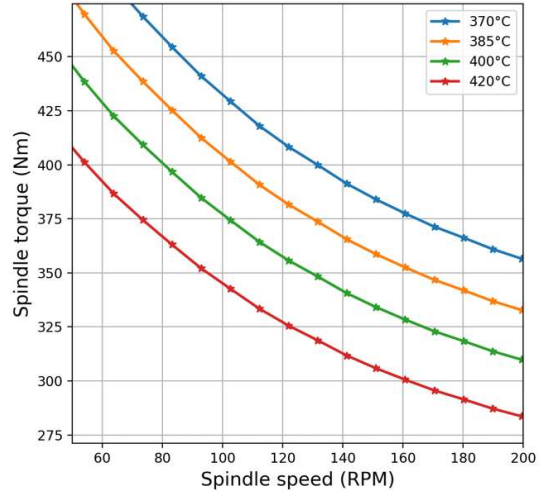


Figure 6: The spindle speed-spindle torque curve is presented for four different temperatures. This curve illustrates the influence of spindle speed and temperature on spindle torque output when spindle speed and temperature are treated as independent variables.

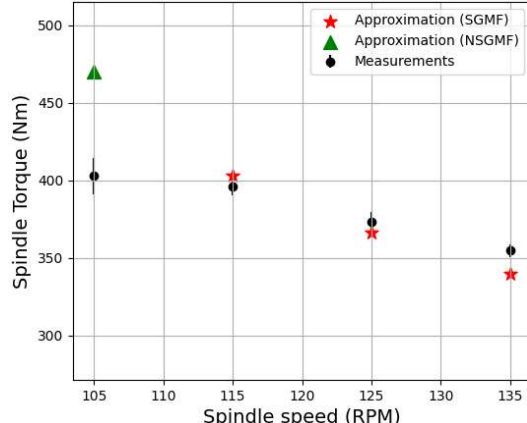


Figure 7: Experimental validation of average spindle torque prediction for Al7075. The average temperature and spindle speed within the time window for model validation are used as inputs. Experiment of 105 RPM has been identified in group NSGMF, which violates model assumption and is not used for model validation. The displayed result of 105 RPM (marked as a triangle) is to show the integrity of model prediction performance on Al7075.

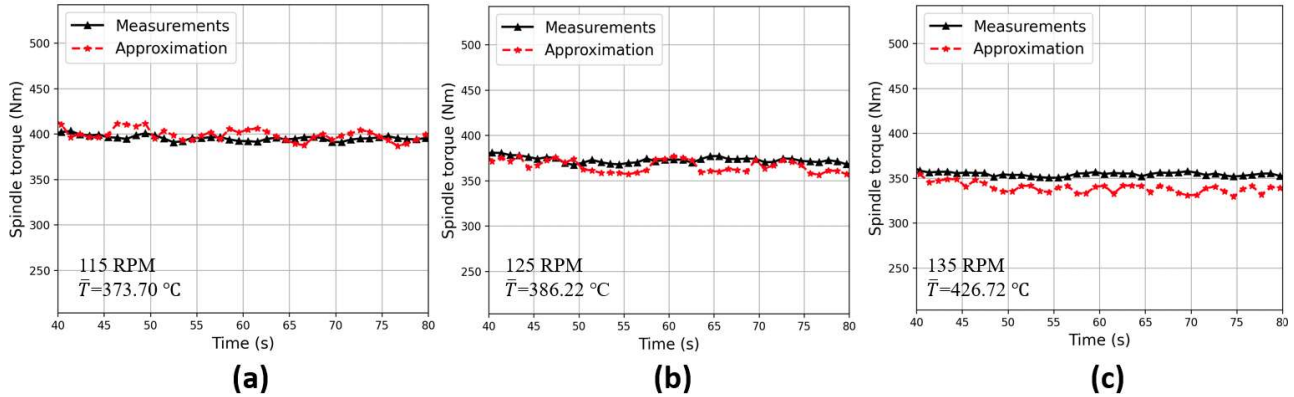


Figure 8: Instantaneous spindle torque for the steady-state deposition. The estimated torque at each timestep is calculated using in-process temperature and spindle speed measurements as inputs. (a) Validation conducted on the data from experiments with a setpoint spindle speed of 115 RPM. (b) Validation conducted on the data from experiments with a setpoint spindle speed of 125 RPM. (c) Validation conducted on the data from experiments with a setpoint spindle speed of 135 RPM.

demonstrated from the following aspects: (1) the effect of slippage on strain rate; (2) the influence of temperature and spindle speed on spindle torque output; (3) average spindle torque prediction using average deposition temperature and spindle speed; and (4) instantaneous spindle torque prediction within the model validation time window using in-process measurements.

Figure 5 illustrates the strain rate at the outer edge of deposition zone under different slip rates. For each spindle speed, the strain rate in this figure is computed from one revolution of tool using Eq. (1) with a specific slip rate. The results show that incorporating slippage has a significant impact on the estimated strain rate for material flow. Notably, substantial overestimations of strain rate can occur when calculations are based solely on tool kinematics. In addition, high strain rates are observed.

Figure 6 shows the spindle speed-spindle torque curve under varying temperatures. It demonstrates how spindle speed and temperature individually influence spindle torque output in the proposed model. The analysis disregards any coupled effects between temperature and spindle speed. It can be observed that thermo-softening effects are predominant. Besides, spindle torque decreases as spindle speed increases for a given temperature. This trend highlights the greater influence of slip rate on torque in the proposed model compared to strain rate hardening in the material constitutive model.

Figure 7 presents the predicted average spindle torque by the proposed model with the combined effects of spindle speed and temperature. Average temperature and spindle speed during the time window for model validation are taken as the inputs. Based on Strategy 1, the experimental data at 105 RPM is identified as the NSGMF case. The results show that the proposed model has good prediction accuracy for SGMF when the model assumptions are met. The prediction deviation of NSGMF may be due to estimating the torque in the deposition zone only based on flow stress, which naturally assumes plastic deformation and becomes invalid when sliding dominates.

The instantaneous spindle torque prediction within the model validation time window for SGMF is shown in Figure 8. Spindle torque is computed using in-process measurements of

spindle speed and temperature at each timestep. Overall, the prediction achieves good alignment with experimental data. Fluctuations between the prediction and experimental data are observed. This could be caused by the nonlinear characteristics of the constitutive model and slip rate, which amplify the effects of spindle speed variations during the steady-state deposition process. The mean absolute percentage error for approximated spindle torque at spindle speeds of 115, 125, and 135 RPM are 1.99%, 2.12%, and 4.29%, respectively.

## 5. Additional Experimental Validation with SS316

Additional validation of the proposed analytical model based on the experimental data of SS316 in the literature is performed. Due to the limited availability of experiments in the literature that simultaneously measure both temperature and spindle torque, the AFSD experiments of SS613 conducted by Agrawal et al. [28] are adopted for further validation. Their work provides a sufficiently detailed experimental setup, making it a suitable case for validation. In [28], a different high strength and work hardening alloy – annealed rod of commercial grade SS316 was deposited under different spindle and traverse speeds. The experiments were performed using MELD-B8® machine and a 38.1 mm diameter W-La<sub>2</sub>O<sub>3</sub> based tool. Details of the process parameters, recorded temperature and spindle torque, measured layer thickness and deposition width are summarized in Table 5. The Johnson-Cook parameters corresponding to SS316 are obtained from the literatures [48-52]. Model parameters for SS316 are set as  $\delta_0 = 3$ ,  $\omega_0 = 400$ , and  $\eta = 0.6$ .

Table 5: Experimental setting and parameters applied for model validation based on SS316 in [28].

Experiments	1	2	3	4
Spindle speed (RPM)	400	600	800	400
Tool traverse speed (mm/s)	4.23	4.23	4.23	3.38
Material feed rate (mm/s)	0.42	0.42	0.42	0.42
Feedstock bar side length (mm)	9.525	9.525	9.525	9.525
Peak temperature (K)	1276.45	1317.96	1348.46	1287.44
Spindle Torque (Nm)	104.7	81.3	59.6	105.0
Commanded deposition height (mm)	0.503	0.503	0.503	0.503
Actual deposition height (mm)	0.441	0.443	0.447	0.445
Measured deposition width (mm)	21.22	21.55	21.55	23.40
Reference slip factor	3	3	3	3
Reference spindle speed (RPM)	400	400	400	400
Scaling factor	0.6	0.6	0.6	0.6

Figure 9 presents the comparison between the predicted and measured spindle torques. Unlike Al7075 where the NSGMF is mainly due to insufficient deposition temperature, the NSGMF of SS316 is mainly caused by the improper ratio of spindle and traverse speeds, where the high traverse speed reduces the time window of tool-material contact. Similarly, it is observed that the model demonstrates good prediction performance for the experimental data in group SGMF.

It should be noted that whether the material flow is sufficiently dragged by the tool is empirically determined in the current work, thus the effective boundary of the proposed model is not fully explored. The model accuracy is expected to be more reliable at higher spindle speeds and lower traverse speeds, where increased temperature and prolonged tool-material contact can enhance material softening and movement. Future exploration is necessary to classify the SGMF under different settings of process parameters, such that an effective range of the proposed model can be provided more rigorously.

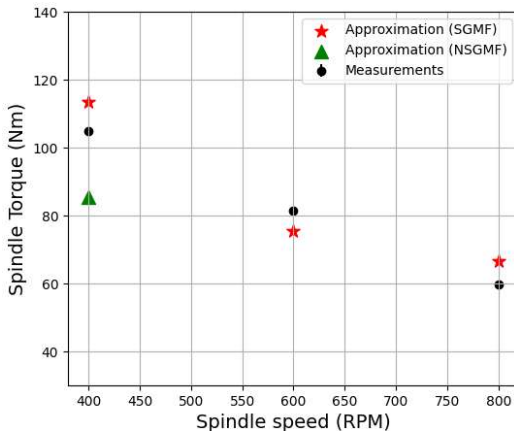


Figure 9: Experimental validation of average spindle torque prediction for SS316. The experiments consisted of the deposition of SS316 under different sets of process parameters. Experiment 1 in Table 5 has been identified in group NSGMF, which violates model assumption and is not used for model validation. The displayed result of experiment 1 (marked as a triangle) is to show the integrity of model prediction performance on SS316.

In summary, experimental validation shows that the proposed analytical model can be generalized to different materials when the material flow is sufficiently generated. This indicates that the established relationship of tool kinematics, material flow, and spindle torque by the proposed analytical model can capture the underlying process physics at tool-material deposition surface in AFSD.

## 6. Conclusions

This paper presents the first analytical model that integrates tool kinematics and material flow for spindle torque prediction in additive friction stir deposition (AFSD). The proposed model can predict steady-state spindle torque for given deposition temperature and process parameters. By addressing the distinct physical processes occurring beneath the feedstock and tool shoulder, the model separately considers the deformation and deposition zones. Material flow is estimated from the kinematics of the rotating-translating tool, that

accounts for slippage. Flow stress is calculated using Johnson-Cook constitutive model, which then informs the torque calculation at the deposition zone. Torque in the deformation zone is estimated based on temperature-dependent yield stress. The combined torque from the deformation and deposition zones accounts for the contributions of plastic deformation and sliding friction to spindle torque. Experiments are performed on wall geometry deposition by AFSD using Al7075 feedstock at different spindle speeds. In addition to Al7075, the experimental data of SS316 in the literature is also applied for model validation. Experimental validation results show that the proposed analytical model can achieve good performance of spindle torque prediction for different deposition materials in AFSD. The proposed analytical model provides an effective interpretation of the physical process at the tool-deposition surface and can enable fast and accurate steady-state spindle torque prediction in AFSD.

Limitations of the proposed analytical model include the assumption of sufficiently generated material flow, leading to the simplifications of contact conditions, such as the temperature effects on slippage. This makes the proposed model not applicable for spindle torque prediction in multi-layer deposition scenarios. In addition, the analytical model cannot adapt to the transition of contact conditions automatically, e.g., the complex transition from sliding-dominant to stabilized slip-stick contact condition. Future work will focus on (1) improving the current model to incorporate influential effects on contact conditions for multi-layer spindle torque prediction and capture the complex transition from sliding-dominant to stabilized slip-stick contact condition; (2) broadening the model capability to include a wider range of process parameters, materials, and tool geometry; and (3) integrating the spindle torque and temperature to develop more accurate thermo-mechanical models for different materials by leveraging its mechanical reflection of the material's resistance to deformation and slip-stick contact condition. The proposed analytical model has the potential to be extended to other additive and hybrid manufacturing processes.

## Acknowledgements

The authors acknowledge support from the NSF Engineering Research Center for Hybrid Autonomous Manufacturing Moving from Evolution to Revolution (ERC-HAMMER) under Award Number EEC-2133630. This work was partially supported by the DOE Office of Energy Efficiency and Renewable Energy (EERE), under contract DE-AC05 00OR22725. The U.S. government retains and the publisher, by accepting the article for publication, acknowledges that the U.S. government retains a nonexclusive, paid-up, irrevocable, worldwide license to publish or reproduce the published form of this manuscript, or allow others to do so, for U.S. government purposes. DOE will provide public access to these results of federally sponsored research in accordance with the DOE Public Access Plan. The authors also gratefully acknowledge the Southeastern Advanced Machine Tools Network (SEAMTN) for partially supporting this research.

## References

- [1] E. Farabi, S. Babaniaris, M.R. Barnett, D.M. Fabijanic, Microstructure and mechanical properties of Ti6Al4V alloys fabricated by additive friction stir deposition, *Additive Manufacturing Letters*, 2 (2022) 100034.
- [2] V. Gopan, K.L.D. Wins, A. Surendran, Innovative potential of additive friction stir deposition among current laser based metal additive manufacturing processes: A review, *CIRP Journal of Manufacturing Science and Technology*, 32 (2021) 228-248.
- [3] R.J. Griffiths, M.E. Perry, J.M. Sietins, Y. Zhu, N. Hardwick, C.D. Cox, H.A. Rauch, H.Z. Yu, A perspective on solid-state additive manufacturing of aluminum matrix composites using MELD, *Journal of Materials Engineering and Performance*, 28 (2019) 648-656.
- [4] S.M. Patil, S. Sharma, S.S. Joshi, Y. Jin, M. Radhakrishnan, N.B. Dahotre, Additive friction stir deposition of Al 6061-B4C composites: Process parameters, microstructure and property correlation, *Materials Science and Engineering: A*, 910 (2024) 146840.
- [5] J. Jordon, P. Allison, B. Phillips, D. Avery, R. Kinser, L. Brewer, C. Cox, K. Doherty, Direct recycling of machine chips through a novel solid-state additive manufacturing process, *Materials & Design*, 193 (2020) 108850.
- [6] G. Stubblefield, M. Williams, M. Munther, J. Tew, R. Rowe, M. Barkey, J. Jordon, P. Allison, Ballistic evaluation of aluminum alloy (AA) 7075 plate repaired by additive friction stir deposition using AA7075 feedstock, *Journal of Dynamic Behavior of Materials*, 9 (2023) 79-89.
- [7] S. Smith, T. Schmitz, T. Feldhausen, M. Sealy, Hybrid metal additive/subtractive machine tools and applications, *CIRP Annals*, 73 (2024) 615-638.
- [8] J. Kincaid, R. Zameroski, E. Charles, T. No, J. Bohling, B. Compton, T. Schmitz, Hybrid manufacturing by additive friction stir deposition, metrology, CNC machining, and microstructure analysis, *Manufacturing Letters*, 35 (2023) 549-556.
- [9] H.Z. Yu, R.S. Mishra, Additive friction stir deposition: a deformation processing route to metal additive manufacturing, *Materials Research Letters*, 9 (2021) 71-83.
- [10] R.J. Griffiths, D. Garcia, J. Song, V.K. Vasudevan, M.A. Steiner, W. Cai, Z.Y. Hang, Solid-state additive manufacturing of aluminum and copper using additive friction stir deposition: Process-microstructure linkages, *Materialia*, 15 (2021) 100967.
- [11] P. Agrawal, R.S. Haridas, S. Yadav, S. Thapliyal, S. Gaddam, R. Verma, R.S. Mishra, Processing-structure-property correlation in additive friction stir deposited Ti-6Al-4V alloy from recycled metal chips, *Additive Manufacturing*, 47 (2021) 102259.
- [12] B. Phillips, C. Mason, S. Beck, D. Avery, K. Doherty, P. Allison, J. Jordon, Effect of parallel deposition path and interface material flow on resulting microstructure and tensile behavior of Al-Mg-Si alloy fabricated by additive friction stir deposition, *Journal of Materials Processing Technology*, 295 (2021) 117169.
- [13] S. Sharma, K.M. Krishna, M. Radhakrishnan, M.V. Pantawane, S.M. Patil, S.S. Joshi, R. Banerjee, N.B. Dahotre, A pseudo thermo-mechanical model linking process parameters to microstructural evolution in multilayer additive friction stir deposition of magnesium alloy, *Materials & Design*, 224 (2022) 111412.
- [14] N. Palya, K. Fraser, Y. Hong, N. Zhu, M. Williams, K. Doherty, P. Allison, J. Jordon, Multi-physics Approach to Predict Fatigue Behavior of High Strength Aluminum Alloy Repaired via Additive Friction Stir Deposition, *Integrating Materials and Manufacturing Innovation*, 12 (2023) 441-455.
- [15] N. Palya, K. Fraser, N. Zhu, J. Hoarston, K. Doherty, P. Allison, J. Jordon, Microstructure prediction from smooth particle hydrodynamics process simulations of additive friction stir deposition, *Metallurgical and Materials Transactions A*, 55 (2024) 3601-3616.
- [16] S.M. Patil, K.M. Krishna, S. Sharma, S.S. Joshi, M. Radhakrishnan, R. Banerjee, N.B. Dahotre, Thermo-mechanical process variables driven microstructure evolution during additive friction stir deposition of IN625, *Additive Manufacturing*, 80 (2024) 103958.
- [17] S.S. Joshi, S. Sharma, M. Radhakrishnan, M.V. Pantawane, S.M. Patil, Y. Jin, T. Yang, D.A. Riley, R. Banerjee, N.B. Dahotre, A multi modal approach to microstructure evolution and mechanical response of additive friction stir deposited AZ31B Mg alloy, *Scientific Reports*, 12 (2022) 13234.
- [18] M. Williams, T. Robinson, C. Williamson, R. Kinser, N. Ashmore, P. Allison, J. Jordon, Elucidating the effect of additive friction stir deposition on the resulting microstructure and mechanical properties of magnesium alloy we43, *Metals*, 11 (2021) 1739.
- [19] G. Stubblefield, K. Fraser, B. Phillips, J. Jordon, P. Allison, A meshfree computational framework for the numerical simulation of the solid-state additive manufacturing process, additive friction stir-deposition (AFS-D), *Materials & Design*, 202 (2021) 109514.
- [20] K.C. Kincaid, D.W. MacPhee, G. Stubblefield, J. Jordon, T.W. Rushing, P. Allison, A finite volume framework for the simulation of additive friction stir deposition, *Journal of Engineering Materials and Technology*, 145 (2023) 031002.
- [21] N. Gotawala, Z.Y. Hang, Material flow path and extreme thermomechanical processing history during additive friction stir deposition, *Journal of Manufacturing Processes*, 101 (2023) 114-127.
- [22] Y. Jin, T. Yang, T. Wang, S. Dowden, A. Neogi, N.B. Dahotre, Behavioral simulations and experimental evaluations of stress induced spatial nonuniformity of dynamic bulk modulus in additive friction stir deposited AA 6061, *Journal of manufacturing processes*, 94 (2023) 454-465.
- [23] T. Shi, J. Wu, M. Ma, E. Charles, T. Schmitz, AFSD-Nets: A Physics-informed machine learning model for predicting the temperature evolution during additive friction stir deposition, *Journal of Manufacturing Science and Engineering*, 146 (2024).
- [24] T. Shi, M. Ma, J. Wu, C. Post, E. Charles, T. Schmitz, AFSD-Physics: Exploring the governing equations of temperature evolution during additive friction stir deposition by a human-AI teaming approach, *Manufacturing Letters*, 41 (2024) 1004-1015.

- [25] Y. Zhu, X. Wu, N. Gotawala, D.M. Higdon, Z.Y. Hang, Thermal prediction of additive friction stir deposition through Bayesian learning-enabled explainable artificial intelligence, *Journal of Manufacturing Systems*, 72 (2024) 1-15.
- [26] T. Schmitz, E. Charles, B. Compton, Analytical temperature model for spindle speed selection in additive friction stir deposition, *Manufacturing Letters*, 41 (2024) 720-729.
- [27] S.S. Joshi, S.M. Patil, S. Mazumder, S. Sharma, D.A. Riley, S. Dowden, R. Banerjee, N.B. Dahotre, Additive friction stir deposition of AZ31B magnesium alloy, *Journal of Magnesium and Alloys*, 10 (2022) 2404-2420.
- [28] P. Agrawal, R.S. Haridas, S. Yadav, S. Thapliyal, A. Dhal, R.S. Mishra, Additive friction stir deposition of SS316: Effect of process parameters on microstructure evolution, *Materials Characterization*, 195 (2023) 112470.
- [29] R.S. Mishra, R.S. Haridas, P. Agrawal, Friction stir-based additive manufacturing, *Science and Technology of Welding and Joining*, 27 (2022) 141-165.
- [30] M.E. Perry, H.A. Rauch, R.J. Griffiths, D. Garcia, J.M. Sietins, Y. Zhu, Y. Zhu, Z.Y. Hang, Tracing plastic deformation path and concurrent grain refinement during additive friction stir deposition, *Materialia*, 18 (2021) 101159.
- [31] D. Garcia, W.D. Hartley, H.A. Rauch, R.J. Griffiths, R. Wang, Z.J. Kong, Y. Zhu, Z.Y. Hang, In situ investigation into temperature evolution and heat generation during additive friction stir deposition: A comparative study of Cu and Al-Mg-Si, *Additive Manufacturing*, 34 (2020) 101386.
- [32] M.A. Aslam, Z. Ke, S.B. Rayhan, M. Faizan, I.M. Bello, An investigation of soft impacts on selected aerospace grade alloys based on Johnson-Cook Material Model, in: *Journal of Physics: Conference Series*, IOP Publishing, 2020, pp. 012008.
- [33] N. Brar, V. Joshi, B. Harris, Constitutive model constants for Al7075 - t651 and Al7075 - t6, in: *Aip conference proceedings*, American Institute of Physics, 2009, pp. 945-948.
- [34] E. Corona, G.E. Orient, An evaluation of the Johnson-Cook model to simulate puncture of 7075 aluminum plates, in, Sandia National Lab.(SNL-NM), Albuquerque, NM (United States), 2014.
- [35] W.K. Rule, S. Jones, A revised form for the Johnson-Cook strength model, *International Journal of Impact Engineering*, 21 (1998) 609-624.
- [36] K. Senthil, M.A. Iqbal, P. Chandel, N. Gupta, Study of the constitutive behavior of 7075-T651 aluminum alloy, *International Journal of Impact Engineering*, 108 (2017) 171-190.
- [37] Z. Wang, Y. Cao, S. Gorbachev, V. Kuzin, W. He, J. Guo, Research on conventional and high-speed machining cutting force of 7075-T6 aluminum alloy based on finite element modeling and simulation, *Metals*, 12 (2022) 1395.
- [38] P. Zhang, J. Liu, Y. Gao, Z. Liu, Q. Mai, Effect of heat treatment process on the micro machinability of 7075 aluminum alloy, *Vacuum*, 207 (2023) 111574.
- [39] W.D. Hartley II, *Processing Mechanics of Additive Friction Stir Deposition*, (2023).
- [40] S. Senkova, O. Senkov, D. Miracle, Cryogenic and elevated temperature strengths of an Al-Zn-Mg-Cu alloy modified with Sc and Zr, *Metallurgical and Materials Transactions A*, 37 (2006) 3569-3575.
- [41] D. Barraclough, H. Whittaker, K. Nair, C.M. Sellars, Effect of specimen geometry on hot torsion test results for solid and tubular specimens, *Journal of testing and evaluation*, 1 (1973) 220-226.
- [42] A. Arora, R. Nandan, A.P. Reynolds, T. DebRoy, Torque, power requirement and stir zone geometry in friction stir welding through modeling and experiments, *Scripta Materialia*, 60 (2009) 13-16.
- [43] D. Andrade, C. Leitão, N. Dialami, M. Chiumenti, D. Rodrigues, Modelling torque and temperature in friction stir welding of aluminium alloys, *International Journal of Mechanical Sciences*, 182 (2020) 105725.
- [44] H. Schmidt, J. Hattel, J. Wert, An analytical model for the heat generation in friction stir welding, *Modelling and simulation in materials science and engineering*, 12 (2003) 143.
- [45] R. Piessens, E. de Doncker-Kapenga, C.W. Überhuber, D.K. Kahaner, Quadpack: a subroutine package for automatic integration, Springer Science & Business Media, 2012.
- [46] Y. Morisada, T. Imaizumi, H. Fujii, Clarification of material flow and defect formation during friction stir welding, *Science and Technology of Welding and Joining*, 20 (2015) 130-137.
- [47] D. Ambrosio, Y. Morisada, K. Ushioda, H. Fujii, Material flow in friction stir welding: A review, *Journal of Materials Processing Technology*, (2023) 118116.
- [48] F. Oviedo, A. Valarezo, Residual stress in high-velocity impact coatings: parametric finite element analysis approach, *Journal of Thermal Spray Technology*, 29 (2020) 1268-1288.
- [49] R. Ghelichi, S. Bagherifard, M. Guagliano, M. Verani, Numerical simulation of cold spray coating, *Surface and Coatings Technology*, 205 (2011) 5294-5301.
- [50] P. Bansal, P. Shipway, S. Leen, Residual stresses in high-velocity oxy-fuel thermally sprayed coatings—Modelling the effect of particle velocity and temperature during the spraying process, *Acta Materialia*, 55 (2007) 5089-5101.
- [51] N. Sawarkar, G. Boob, Finite element based simulation of orthogonal cutting process to determine residual stress induced, *Int. J. Comput. Appl.*, 975 (2014) 8887.
- [52] N.E. Karkalos, A.P. Markopoulos, Determination of Johnson-Cook material model parameters by an optimization approach using the fireworks algorithm, *Procedia Manufacturing*, 22 (2018) 107-113.